



CHORUS

This is the accepted manuscript made available via CHORUS. The article has been published as:

Charge density wave modulation in superconducting BaPbO₃/BaBiO₃ superlattices

D. T. Harris, N. G. Campbell, C. Di, J.-M. Park, L. Luo, H. Zhou, G.-Y. Kim, K. Song, S.-Y. Choi, J. Wang, M. S. Rzchowski, and C. B. Eom

Phys. Rev. B **101**, 064509 — Published 19 February 2020

DOI: [10.1103/PhysRevB.101.064509](https://doi.org/10.1103/PhysRevB.101.064509)

Charge Density Wave Modulation in Superconducting BaPbO₃/BaBiO₃ Superlattices

D. T. Harris,¹ N. Cambell,² C. Di,³ J.-M. Park,³ L. Luo,³ H. Zhou,⁴ G.-Y. Kim,⁵ K. Song,⁵ S.-Y. Choi,⁵ J. Wang,³ M. S. Rzchowski,² and C. B. Eom^{1*}

¹*Department of Materials Science and Engineering, University of Wisconsin-Madison, Madison, Wisconsin 53706, USA.*

²*Department of Physics, University of Wisconsin-Madison, Madison, Wisconsin 53706, USA.*

³*Department of Physics and Astronomy and Ames Laboratory-U.S. DOE, Iowa State University, Ames, Iowa 50011, USA*

⁴*Advanced Photon Source, Argonne National Laboratory, Argonne, Illinois 60439, USA*

⁵*Department of Materials Science and Engineering, POSTECH, Pohang 37673, South Korea.*

The isotropic, non-magnetic doped BaBiO₃ superconductors maintain some similarities to high- T_c cuprates, while also providing a cleaner system for isolating charge density wave (CDW) physics that commonly competes with superconductivity. Artificial layered superlattices offer the possibility of engineering the interaction between superconductivity and CDW. Here we stabilize a low temperature, fluctuating short range CDW order by using artificially layered epitaxial (BaPbO₃)_{3m}/(BaBiO₃)_m ($m = 1-10$ unit cells) superlattices that is not present in the optimally doped BaPb_{0.75}Bi_{0.25}O₃ alloy with the same overall chemical formula. Charge transfer from BaBiO₃ to BaPbO₃ effectively dopes the former and suppresses the long range CDW, however as the short range CDW fluctuations strengthens at low temperatures charge appears to localize and superconductivity is weakened. The monolayer structural control demonstrated here provides compelling implications to access controllable, local density-wave orders absent in bulk alloys and manipulate phase competition in unconventional superconductors.

*Correspondence to: eom@engr.wisc.edu

Keywords: Superconductivity, Charge density wave, Superlattice, Thin Films

The properties of quantum materials are often determined by multiple distinct order parameters that represent the importance of coupled and competing phases. The high- T_c cuprates exhibit a rich phase diagram with magnetic and electronic phases that are commonly thought to compete with the emergence of superconductivity [1]. In addition to magnetic ordering, recently discovered striped charge ordering in cuprates appears to compete with superconductivity in a manner reminiscent of the emergent charge density wave (CDW) seen in other superconductors [2]. Doped BaBiO_3 (BBO) superconductors possess a commensurate CDW in the parent compound, stable to high temperatures, in an isotropic, nonmagnetic complex oxide. The CDW manifests as bond disproportionation through a frozen breathing mode of the BiO_6 octahedra, as pictured in Figure 1(a), with recent experimental and first principle work suggesting hybridization of the BiO_6 octahedra plays a dominate role [3–6]. Doping BBO with Pb in $\text{BaPb}_{1-x}\text{Bi}_x\text{O}_3$ (BPBO, $T_c=11$ K) or K in $\text{Ba}_{1-x}\text{K}_x\text{BiO}_3$ (BKBO, $T_c=30$ K) destroys the long range CDW [7–9]. However, Raman and terahertz measurements of bulk single crystals suggest short range CDW fluctuations persist on the Bi-rich, underdoped side of the superconducting dome of BPBO and could influence both the normal state and superconducting properties [10,11].

The CDW and monoclinic distortion in BBO are similar to those found in the rare-earth nickelates [12,13], a class of materials heavily explored for possible high- T_c superconductivity analogous to the cuprates and predicted to display high- T_c superconductivity when grown in artificial superlattices [14]. While these non-cuprate superconductors have not been demonstrated, artificial superlattices of complex oxides can stabilize non-equilibrium phases that exhibit enhanced properties or novel phases for a wide variety of functional systems not accessible by their bulk counterparts [15]. For example, manganite-cuprate superlattices manipulate the charge-ordering phase and control electron-phonon coupling between layers [16,17]. Similarly, here we successfully stabilize, a short-range CDW order in artificial $(\text{BaPbO}_3)_{3m}/(\text{BaBiO}_3)_m$ superconducting superlattices with the same overall composition as the optimally doped $\text{BaPb}_{0.75}\text{Bi}_{0.25}\text{O}_3$ alloy that otherwise does not exhibit this same order. The superconducting samples show a remarkably strong temperature and superlattice period dependent CDW signature in Raman measurements due in part to charge transfer between BBO and BaPbO_3 (BPO) layers. This is distinct from conventional Raman modes in the BPBO alloy that show a very weak temperature dependence [10, 20]. The enhancement of the short range

CDW fluctuations at low temperatures, exclusively in superlattices, is shown to increase the tendency of charge localization and weaken the superconductivity. The tuning method demonstrated here by monolayer engineering provides a platform that the competing electronic order and its fluctuations at small scales can be tailored for both elucidating the mechanisms of unconventional superconductivity and access short range emergent orders. The compelling implications may impact the entire field of emergent materials phase discovery and control.

We grew $\text{BPO}_{3m}/\text{BBO}_m$ superlattices using 90° off-axis magnetron sputtering, with the BPO:BBO fixed at 3:1, the optimal doping in the random alloy system. The total sample thickness is fixed at ~ 85 nm to avoid thickness related disorder effects when characterizing superconductivity [18]. We characterized film quality using laboratory and synchrotron x-ray diffraction (XRD), atomic force microscopy (AFM), and scanning transmission electron microscopy (STEM) [21]. Figure 1 shows characterization of our superlattice quality. Out-of-plane 2θ - θ scans exhibit a single film peak and clear Kiessig fringes originating from the uniformity of the overall film thickness. All superlattices show additional satellite reflections arising from the artificial periodicity in our grown samples, and these superlattice reflections and thickness fringes are well matched by simulations of our film (Fig. 1 (c)), which underscore the high structural quality of the superlattice samples. The out-of-plane rocking curve shows a full width at half maximum of 0.020° , indicative of the high of crystalline quality of our samples. AFM, Fig. 1(d), reveals a smooth surface with RMS of 0.5 nm and a step-terrace structure. Reciprocal space maps of the 103_{pc} reflection reveal relaxation of the film with respect to the substrate, expected due to the large lattice constants of BBO (~ 4.36 Å) and BPO (~ 4.25 Å), giving on the order of 10% lattice mismatch with SrTiO_3 .

Due to the extreme electron beam sensitivity of BBO materials, atomic-resolution transmission electron microscopy quickly degraded the films making reliable chemical mapping challenging [19, 21]. We therefore performed STEM characterization of $\text{BaBiO}_3/\text{BaPbO}_3$ together with crystal truncation rod (CTR)/coherent Bragg rod analysis (COBRA) to resolve the interfacial width between the BBO and BPO layers. Low-resolution TEM, shown in Fig 2(a), reveals well-separated layers, however the similarity of the two constituent materials limits atomic number contrast between the two layers. For this reason, we carried out CTR measurements slightly beneath the Pb L_3 absorption edge to enhance the atomic-form-factor

contrast between the Bi and Pb elements [21]. The CTR measurements were performed on thinner BPO/BBO/BPO trilayer samples to allow subsequent COBRA analysis to determine the interfacial width. In Figs. 2(b) and 2(c), the COBRA-derived total electron density profile and integrated electron number in the B-site atomic layer exhibit a relatively sharp BPO/BBO interface (less than 2 unit cells in width) suggesting a limited intermixing of Pb and Bi across the interface, which further confirms the superlattice quality that gives rise to satellite peaks and places limits on the amount of interdiffusion that could lead to extrinsic effects.

Figs. 3(a) and 3(b) plot temperature dependence of carrier densities extracted from Hall measurements and transition temperatures extracted from resistivity measurements, respectively. Specifically, superlattices with small period ($m=1,2,3$) show zero resistivity and onset of a diamagnetic signal at low temperature, as shown in Figs. 3(c) and 3(d), confirming superconductivity in our superlattices. The resistive transitions are broad and multistep, possible evidence of a granular nature to the superconductivity. Samples with larger period ($m=10, 17$) do not show superconductivity above 2K, the temperature dependent resistivity and Hall carrier density remain nearly constant from room temperature to 2 K, and the behavior and the values for n_{3D} closely match a reference BPO film, indicating large period films with low interfacial density behave as independent layers. In contrast, as the lattice modulation period m decreases, the temperature dependent behavior of the superlattices reveals distinct differences from the bulk alloyed reference sample and possible indication of trapping of mobile charge. This trapping is seen in the more negative $d\rho/dT$ and drop in Hall n_{3D} at 40 K for $m=1,2,3$ samples, and could be related to strengthening of a short range CDW that is discussed below. The room temperature n_{3D} increases smoothly as m is decreased and the number of interfaces increases, consistent with approximately half an electron per formula unit transferred at each interface. This means that the electron concentration in the BaBiO₃ layer increases as the period of the superlattice decreases.

Further evidence for charge transfer between the layers can be found in optical reflectivity spectra shown in Figs. 4(a) and 4(b). For a BBO control sample, a strong maximum appears in optical reflectivity spectra which is a characteristic of a well-defined oscillator from the CDW mode. For $m=2$ and 5, the optical reflectivity spectra with minima around 2 eV and sharp rise in the low-energy region indicate a low-frequency spectral weight in the form of a carrier plasma. This indicate that the charge transfer occurring in $m=2$ and $m=5$ films effectively

dopes the BBO layer and suppress the long range CDW order. **This corroborates our conclusion that the superconductivity is driven by charge transfer between the BBO and BPO layers.** A model calculation consisting of the dielectric function of the CDW gap for BBO and a Drude carrier plasma term for the metallic film on substrate [21] reproduces the experimentally determined optical reflectivity, as shown in Fig. 4(b). Lowering layer thickness m increases charge transfer between layers, i.e., the blueshift of the plasma edge in Fig. 4(a), possibly due to interlayer proximity and coupling, leading to higher carrier density, fully in agreement with the Hall measurements (Fig. 3(a)).

To understand how charge transfer modulates the CDW, we next present temperature and superlattice period dependent Raman scattering measurements which provide evidence for the formation of a short range CDW order competing with superconductivity. The Raman spectra from $\text{BPO}_{3m}/\text{BBO}_m$ superlattices are presented in Figs. 4(c) and 4(d) for different $m=1, 2, 3,$ and 10 together with control samples from BPBO and BBO films, and a STO substrate at 4.2K and 785 nm(Fig. 4(c)). A fully gapped, long-range CDW state in BBO (gray line) gives rise to a sharp Raman active phonon breathing mode at 569 cm^{-1} [19], which in the $m=10$ superlattice shows a smaller intensity and broader linewidth. Further decreases in m completely suppress the 569 cm^{-1} peak at room temperature, yet, most intriguingly, the spectral weight of the CDW appears to persist at low temperatures as a broad spectral resonance near 550 cm^{-1} , even for samples showing superconductivity, e.g., as seen in $m=3$ (black line) and 2 (red line) traces. We emphasize three key properties of the “residual” spectral mode seen in the Raman spectra:

(1) It exhibits remarkably strong temperature dependence. The $m=3$ sample (black line) in Fig. 4(d) shows a featureless spectral profile near 550 cm^{-1} close to room temperature that resembles the STO substrate (orange line). By removing the scattering contribution from the STO substrate in the measured spectral range of $430\text{-}680 \text{ cm}^{-1}$, normalized $I(T)/I(300\text{K})$ spectra, shown Fig. 4(e) and its top panel, clearly demonstrate the strong suppression of the residual Raman mode at elevated temperatures. Several broad resonances above 200 cm^{-1} were seen and assigned as two-phonon scattering modes in the bulk single-crystal BPBO [20]. However, these modes only exhibit a very weak temperature dependence with large scattering intensity at room temperature which cannot account for the strikingly sensitive temperature tuning of the presently observed residual Raman mode.

(2) The broad, Raman spectral shape in Fig. 4(e) is characteristic of two resonant modes at 598 cm^{-1} and 545 cm^{-1} , marked by two dashed lines. The 598 cm^{-1} peak has been assigned to the breathing mode of BiO_6 octahedra [19], which has the same origin as the 569 cm^{-1} CDW mode in BBO in Pb-doped metallic compounds. The energy increase and spectral lineshape change are likely due to the decrease of the Bi-O bond length [20] and/or the electron-phonon renormalization. Therefore, in the absence of the sharp CDW peak from the long-range order, these distinct monolayer number m and temperature dependences of the residual resonances provide a compelling evidence for the existence of short-range CDW correlations for samples showing superconductivity. This local electronic order strongly renormalizes the breathing mode that gives rise to the persisting spectral weight with a strong temperature dependence absent in bulk single crystal BPBO [19, 20].

(3) The strong m dependence of the residual spectral weight further demonstrates the monolayer thickness control of CDW fluctuations in our superlattice systems. This is clearly seen in Fig. 4(c) where the residual Raman mode for $m=3$ (black) is significantly larger than both $m=1$ (blue) and BPBO bulk alloy (green) samples. Prior studies of bulk single crystals related optical spectra and pseudogap formation with a spatially-temporally fluctuating short-range CDW order of a few unit cells in BiO_6 octahedra on the Bi-rich, underdoped side of the BPBO phase diagram [10, 11], which is consistent with our proposed physical mechanism here. It is critical note, however, that such short range CDW is not present in the optimally doped $\text{BaPb}_{0.75}\text{Bi}_{0.25}\text{O}_3$ alloy with the same overall chemical formula as our superlattice samples.

Finally, we note that the CDW is not only influenced by the thickness of BBO layer but also driven by charge transfer between the BBO and BPO layers as we extensively discussed in Figs. 3 and 4. The latter can only be studied by developing artificially layered epitaxial $(\text{BaPbO}_3)_{3m}/(\text{BaBiO}_3)_m$ superlattices instead of bulk alloys. Although the superlattices have the same overall chemical formula as the optimally doped $\text{BaPb}_{0.75}\text{Bi}_{0.25}\text{O}_3$ alloy, our results provide compelling evidence for a low temperature, fluctuating short range CDW order that is not in the bulk compound as discussed in Raman data of Figs. 3(c)-3(e), which we attribute to the charge transfer from BaBiO_3 to BaPbO_3 .

This work demonstrates structural and electronic engineering of a model system $\text{BPO}_{3m}/\text{BBO}_m$ at the monolayer limit for understanding CDW that competes with

superconductivity. The design and discovery of previously-unestablished superlattices allow the manipulation of the CDW and its fluctuations by controlling charge transfer. This hints at additional quantum control of hidden phases by combining with other complementary tuning methods [25, 26].

Acknowledgements

Synthesis, characterization, and analysis at UW-Madison were supported with funding from the Department of Energy Office of Basic Energy Sciences under award number DE-FG02-06ER46327. The work at Ames Laboratory and Iowa State University (Raman and optical spectroscopy characterizations and analysis) was supported by the DOE Office of Science, Basic Energy Sciences, Materials Science and Engineering Division. Ames Laboratory is operated for the DOE by Iowa State University under Contract No. DE-AC02-07CH11358. This research used resources of the Advanced Photon Source, a U.S. Department of Energy (DOE) Office of Science User Facility operated for the DOE Office of Science by Argonne National Laboratory under Contract No. DE-AC02-06CH11357.

References

- [1] M. Vojta, *Adv. Phys.* **58**, 699 (2009).
- [2] J. Chang, E. Blackburn, A. T. Holmes, N. B. Christensen, J. Larsen, J. Mesot, R. Liang, D. A. Bonn, W. N. Hardy, A. Watenphul, M. v. Zimmermann, E. M. Forgan, and S. M. Hayden, *Nat. Phys.* **8**, 871 (2012).
- [3] A. P. Menushenkov and K. V. Klementev, *J. Phys. Condens. Matter* **12**, 3767 (2000).
- [4] K. Foyevtsova, A. Khazraie, I. Elfimov, and G. A. Sawatzky, *Phys. Rev. B* **91**, 121114(R) (2015).
- [5] S. Balandeh, R. J. Green, K. Foyevtsova, S. Chi, O. Foyevtsov, F. Li, and G. A. Sawatzky, *Phys. Rev. B* **96**, 165127 (2017).
- [6] A. Khazraie, K. Foyevtsova, I. Elfimov, and G. A. Sawatzky, *Phys. Rev. B* **97**, 075103 (2018).
- [7] A. W. Sleight, J. L. Gillson, and P. E. Bierstedt, *Solid State Commun.* **17**, 27 (1975).
- [8] R. J. Cava, B. Batlogg, J. J. Krajewski, R. Farrow, L. W. Rupp, a. E. White, K. Short, W. F. Peck, and T. Kometani, *Nature* **332**, 814 (1988).
- [9] A. W. Sleight, *Phys. C* **514**, 152 (2015).
- [10] S. Tajima, S. Uchida, A. Masaki, H. Takagi, K. Kitazawa, S. Tanaka, and A. Katsui, *Phys. Rev. B* **32**, 6302 (1985).
- [11] D. Nicoletti, E. Casandruc, D. Fu, P. Giraldo-Gallo, I. R. Fisher, and A. Cavalleri, *Proc. Natl. Acad. Sci.* **114**, 9020 (2017).
- [12] S. Johnston, A. Mukherjee, I. Elfimov, M. Berciu, and G. A. Sawatzky, *Phys. Rev. Lett.* **112**, 106404 (2014).
- [13] J. Shamblin, M. Heres, H. Zhou, J. Sangoro, M. Lang, J. Neuefeind, J. A. Alonso, and S. Johnston, *Nat. Commun.* **9**, 86 (2018).
- [14] J. Chaloupka and G. Khaliullin, *Phys. Rev. Lett.* **100**, 016404 (2008).
- [15] H. Y. Hwang, Y. Iwasa, M. Kawasaki, B. Keimer, N. Nagaosa, and Y. Tokura, *Nat. Mater.* **11**, 103 (2012).
- [16] N. Driza, S. Blanco-Canosa, M. Bakr, S. Soltan, M. Khalid, L. Mustafa, K. Kawashima, G. Christiani, H.-U. Habermeier, G. Khaliullin, C. Ulrich, M. Le Tacon, and B. Keimer, *Nat. Mater.* **11**, 675 (2012).
- [17] A. Frano, S. Blanco-Canosa, E. Schierle, Y. Lu, M. Wu, M. Bluschke, M. Minola, G. Christiani, H. U. Habermeier, G. Logvenov, Y. Wang, P. A. van Aken, E. Benckiser, E. Weschke, M. Le Tacon, and B. Keimer, *Nat. Mater.* **15**, 831 (2016).
- [18] D. T. Harris, N. Campbell, R. Uecker, M. Brützam, D. G. Schlom, A. Levchenko, M. S. Rzchowski, and C.-B. Eom, *Phys. Rev. Mater.* **2**, 041801 (2018).
- [19] H. G. Lee, R. Kim, J. Kim, M. Kim, T. H. Kim, S. Lee, and T. W. Noh, *APL Mater.* **6**, 016107 (2018).

- [20] S. Sugai, S. Uchida, K. Kitazawa, S. Tanaka, and A. Katsui, *Phys. Rev. Lett.* **55**, 426 (1985).
- [21] See Supplemental Material at [URL will be inserted by publisher] for additional synthesis and characterization details.
- [22] E. D. Palik, *Handbook of Optical Constants of Solids* (Academic Press, London, 1997).
- [23] O. S. Heavens, *Optical Properties of Thin Solid Films* (Dover Publications, Inc., New York, 1991).
- [24] G. Kim, M. Neumann, M. Kim, M. D. Le, T. D. Kang, and T. W. Noh, *Phys. Rev. Lett.* **115**, 226402 (2015).
- [25] G. Campi, A. Bianconi, N. Poccia, G. Bianconi, L. Barba, G. Arrighetti, D. Innocenti, J. Karpinski, N. D. Zhigadlo, S. M. Kazakov, M. Burghammer, M. v Zimmermann, M. Sprung, and A. Ricci, *Nature* **525**, 359 (2015).
- [26] X. Yang, C. Vaswani, C. Sundahl, M. Mootz, P. Gagel, L. Luo, J. H. Kang, P. P. Orth, I. E. Perakis, C. B. Eom, and J. Wang, *Nat. Mater.* **17**, 586 (2018).
- [27] P. H. Tan, W. P. Han, W. J. Zhao, Z. H. Wu, K. Chang, H. Wang, Y.F. Wang, N. Bonini, N. Marzari, N. Pugno, and G. Savini, *Nat. Mater.* **11**, 294 (2012).

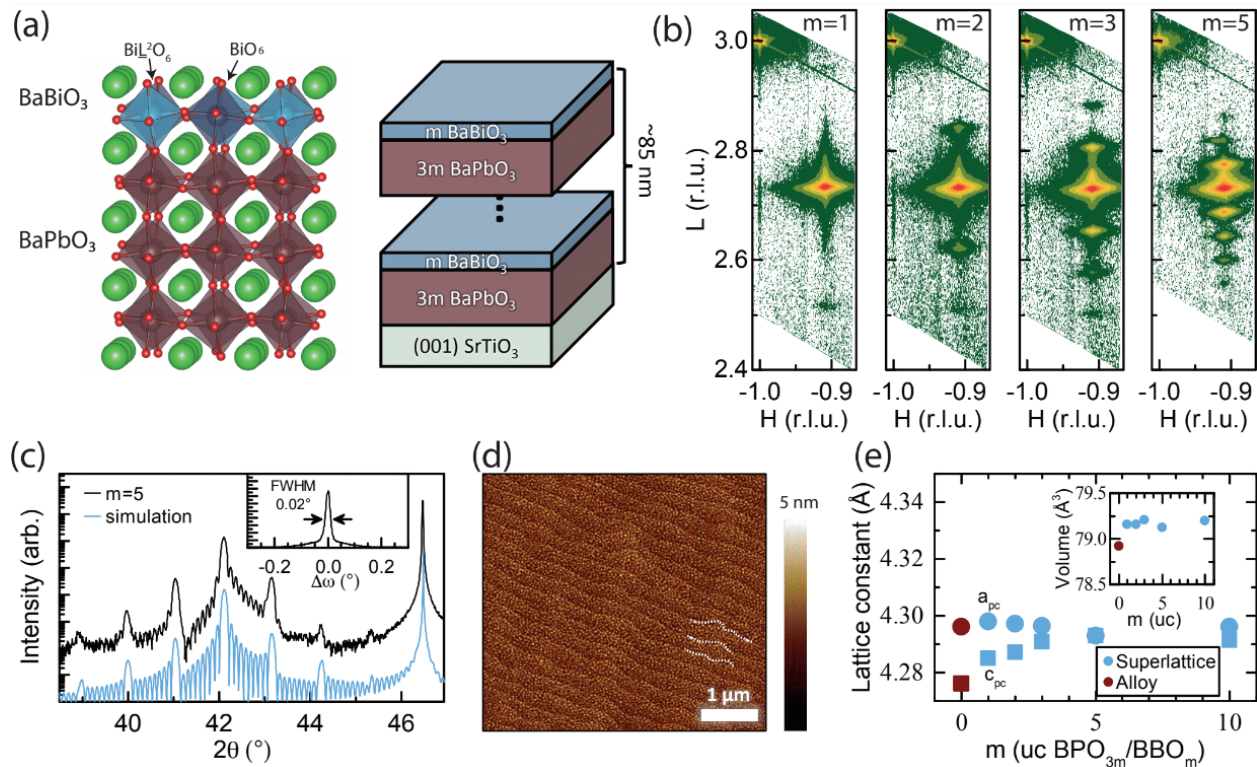


Figure 1. Superlattice characterization. (a) Schematic of BaBiO₃, BaPbO₃, and superlattice structures. (b) Reciprocal space maps around the 103_{pc} reflection for m=1, 2, 3, and 5 superlattices. Satellite superlattice reflections are visible for all samples. (c) Out-of-plane 2θ-θ scan of an m=5 sample showing clear Kiessig fringes and superlattice reflections with excellent agreement with the pattern simulation. The inset shows the out-of-plane rocking curve of the film reflection. (d) Atomic force microscopy image of the surface topography. The white dashed lines highlight step edges. (e) In-plane and out-of-plane pseudocubic lattice parameters extracted from reciprocal space maps. The inset shows the unit cell volume.

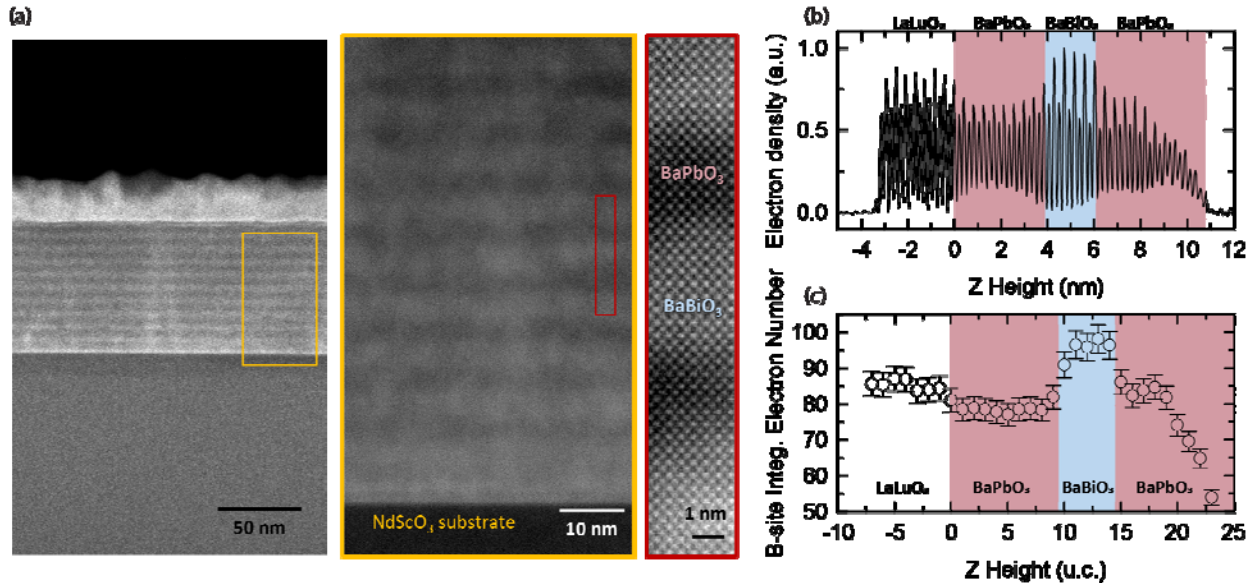


Figure 2. TEM characterization of BaBiO₃/BaPbO₃ and chemical interfacial width and intermixing at the interfaces resolved by the resonant coherent Bragg rod analysis method. (a) Low and high resolution STEM images. (b) Resonant COBRA-derived electron density profile of a BaPbO₃/BaBiO₃/BaPbO₃ trilayer sample. (c) Resonant COBRA-derived integrated electron number in each perovskite B-site atomic layer along the out-of-plane direction.

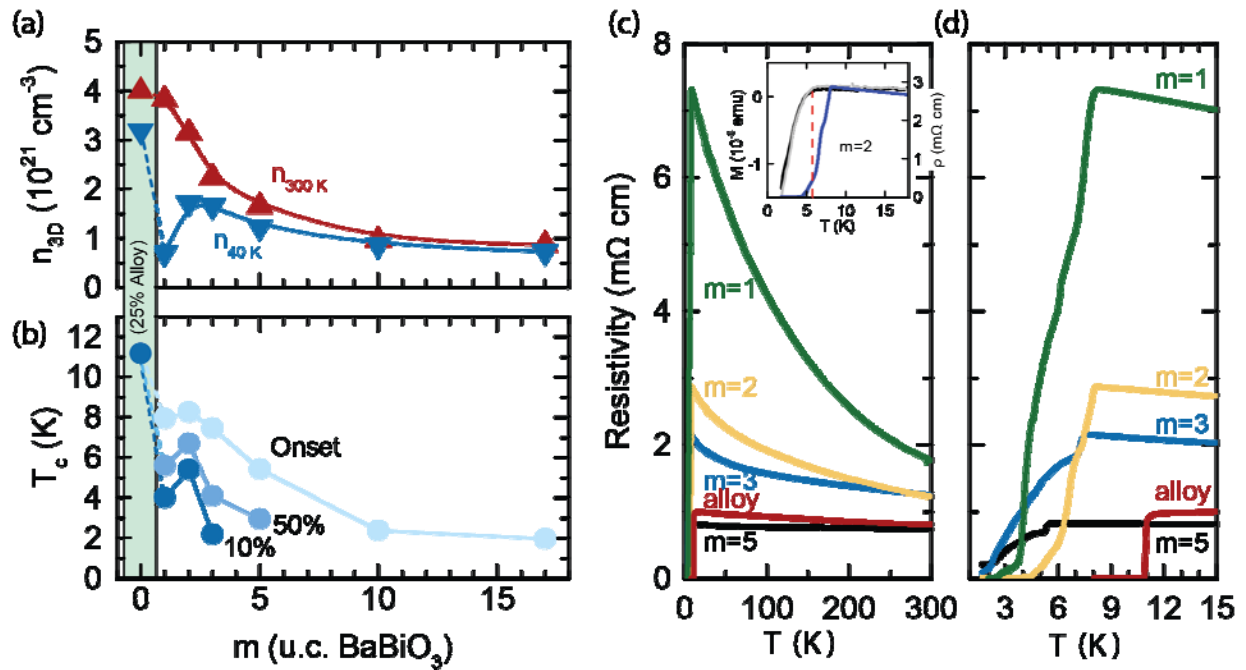


Figure 3. Transport characterization. (a) Room and low temperature 3D carrier densities extracted from Hall measurements. (b) Transition temperatures extracted from resistivity measurements. (c) Full temperature range resistivity vs. temperature. The inset of (c) overlays the transition probed by resistive measurements (blue) with out-of-plane (black) and in-plane (grey) onset of diamagnetism (red dashed line) for $m=2$. (d) Transition region of superconducting samples.

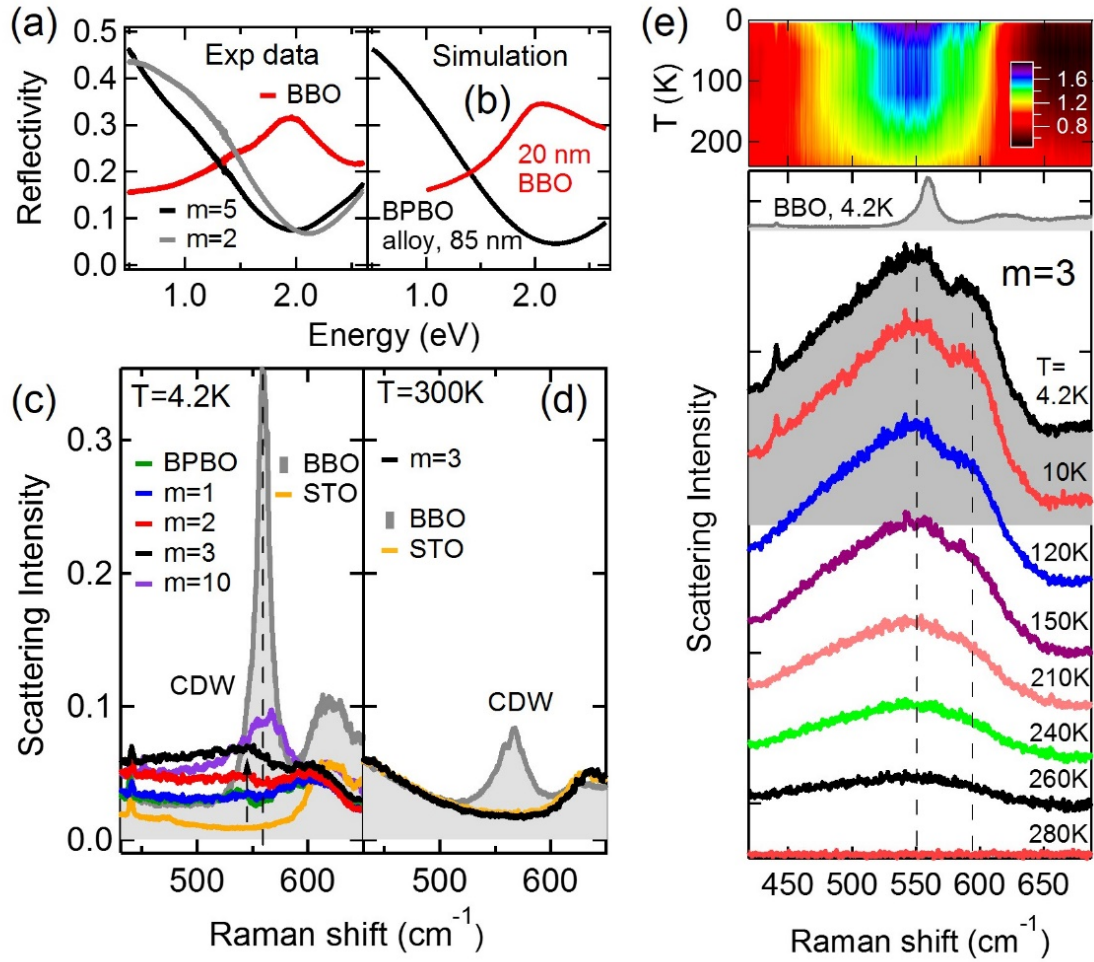


Figure 4. Optical and Raman spectroscopy characterizations. (a) Experimental reflectivity data for BBO and for $m=2$ and 5 superlattices. (b) Simulation of the optical spectra [21-23]. (c) Low temperature Raman measurements around the CDW peak (dashed line) for selected superlattices, reference BBO and BPBO films, and STO substrate. The charge transfer (main text) suppresses the sharp CDW peak to a broad cusp shape of spectrum (black arrow). (d) Room temperature Raman measurements in an $m=3$ superlattice. (e) Normalized low temperature Raman spectra ($I(T)/I(300K)$) around the CDW peaks for the $m=3$ sample. The traces are offset for clarity.